Exploring Copper β-Diketiminate Complexes for Heterogeneous Ammonia Oxidation Anchored on Graphitic Surfaces via CH-π and π-π Interactions

Josep A. Gutiérrez-Orgaz[1], Marco Nicaso[1], Anna M. Beiler[1], Marta Martínez-Belmonte[1], Jordi Benet-Buchholz[1], Mireia Segado-Centellas[1,2], Xavier Sala[3], Carles Bo[1,2], and Antoni Llobet[,1]*

[1] Institute of Chemical Research of Catalonia (ICIQ), Barcelona Institute of Science and Technology (BIST), Avda. Països Catalans, 16, 43007 Tarragona, Spain.

[2] Departament de Química Física i Inorgànica, Universitat Rovira i Virgili (URV), Marcel·lí Domingo s/n, 43007 Tarragona, Spain

[3] Departament de Química, Universitat Autònoma de Barcelona (UAB), 08193 Cerdanyola del Vallès, Spain

ABSTRACT

Ammonia is a compelling candidate for a carbon-free energy carrier, offering potential applications as both a hydrogen vector and a fuel. Unlocking these applications requires the development of efficient ammonia oxidation catalysts. Building on recent work with a fluorinated Cu(I) *β*-diketiminate catalyst for homogeneous ammonia oxidation, we present the first examples of hybrid electrodes employing first-row metal complexes and supramolecular anchoring for heterogeneous ammonia oxidation. In this study, we developed innovative synthetic methodologies to produce a family of *β*-diketiminate ligands and complexes. Some analogues clarified the role of each functional group in the original ligand, while others incorporated moieties designed to facilitate immobilization on graphitic surfaces via CH-π and π-π interactions. These structural modifications not only broadened the scope of ligand design but also advanced our understanding of their roles in catalysis and immobilization. Unexpectedly, all synthesized Cu complexes, including the previously reported catalyst, formed an equilibrium with $[Cu^{I}(NH_3)_4]^+$ or $[Cu^{II}(NH_3)_4]^+$ in the presence of ammonia, leading to ligand dissociation and subsequent catalyst deactivation. Despite these challenges, we demonstrated that anchoring these complexes is feasible and confirmed that heterogeneous ammonia oxidation is possible with this system. This work represents a pivotal step toward the construction of ammonia oxidation systems based on earth-abundant metals, highlighting the promise of Cu *β*-diketiminate complexes. Addressing the challenges of ligand loss and catalyst stability will pave the way for robust and efficient systems, driving advancements in sustainable ammonia-based energy technologies.

TOC Image.

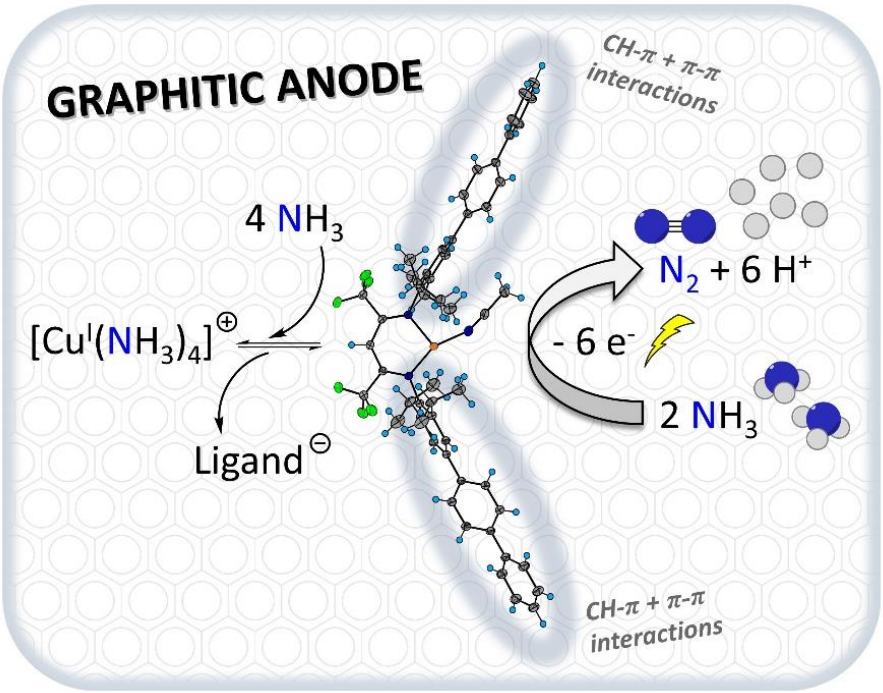

KEYWORDS. Ammonia oxidation, CH-π interactions, redox catalysis, molecular electrocatalysis, heterogeneous catalysis, *β*-diketiminate complexes

INTRODUCTION

The massive anthropogenic use of fossil fuels over recent decades has significantly contributed to the rise in Earth's temperature, a phenomenon known as global warming.[1,2] This temperature increase has, in turn, triggered extreme climate events, intensifying the global climate crisis we face today.[3–5] It is thus imperative and urgent to start the transition from fossil to clean and sustainable energy sources such as solar fuels.[6]

In this context ammonia stands out as a potential solar fuel vector due to its relatively high energy density,[7] low flammability, and ease of liquefaction, making it well-suited for transport through the existing global logistics infrastructure.[8,9] Moreover, ammonia is especially attractive as a fuel because it is carbon-free, positioning it as an environmentally friendly energy solution.[10]

To harness ammonia as a fuel, catalysts capable of efficiently and selectively facilitating the ammonia oxidation reaction are essential for designing practical ammonia-based fuel cell technologies (Equation 1).[11–15]

$$4\ NH_3 + 3\ O_2 \rightleftharpoons 2\ N_2 + 6\ H_2O;\ E^o = 0.68\ V \quad (1)$$

$$2\ NH_3 \rightleftharpoons N_2 + 3\ H_2;\ E^o = -0.55\ V \quad (2)$$

$$8\ NH_3 + 3\ CO_2 \rightleftharpoons 4\ N_2 + 3\ CH_4 + 6\ H_2O;\ E^o = -0.38\ V \quad (3)$$

$$4\ NH_3 + 2\ CO_2 \rightleftharpoons 2\ N_2 + C_2H_4 + 4\ H_2O;\ E^o = -0.49\ V \quad (4)$$

Additionally, ammonia can serve as a source of hydrogen (Equation 2), which can then be used to generate energy in situ.[16,17] Furthermore, when combined with CO_2 reduction, ammonia can be utilized to produce carbon-neutral fuels such as methane (Equation 3),[18,19] or valuable industrial

synthons, like ethylene (Equation 4).[20] For these technological applications to be feasible, catalysts are required for the reactions outlined in Equations 1-4.[9,21,22]

In homogenous phase, a limited number of molecular catalysts based on transition metal complexes of Mn[23], Ni[24], Cu[25–27], Fe[28–34] and Ru[35–46] have been explored for ammonia oxidation, although their performance is often constrained by both stability and effectiveness.[21,47] Moreover, solid-state photo(electro)anodes and cathodes are needed to significantly simplify the operation of photo(electro)chemical cells. To achieve this, it is essential to robustly anchor the molecular catalyst onto solid conductive and/or semiconductive surfaces.

Anchoring well-defined molecular catalysts onto solid supports offers significant advantages over both traditional homogeneous and heterogeneous catalysts. A key benefit is the minimal amount of catalyst required, which enables uniform activity across the entire solid support. This contrasts with conventional drop-casting methods, which typically lead to an inhomogeneous dispersion of active centers and necessitate larger amounts of catalyst. Additionally, in drop-casting, only a small fraction of the deposited catalyst is active, as most of it does not come into contact with the electrolyte solution.[48] From an environmental standpoint, anchoring of molecular catalysts via supramolecular interactions, rather than covalent bonds, represents a significant step toward more sustainable technologies in the chemical sector, due to its reduced environmental impact.[49]

Recently, we reported the first successful example of a molecular hybrid material where a molecular Ru ammonia oxidation catalyst was anchored on graphitic surfaces via CH-π interactions.[44,50] Building on this, we now turn our focus to anchoring ammonia oxidation catalysts based on first-row transition metals using a similar immobilization strategy. For this purpose, we

have selected the recently reported *β*-diketiminate complex **[Cu^{I}(L2)(MeCN)]**[27] (Scheme 2), which has been proposed to oxidize ammonia to dinitrogen in homogeneous phase. To facilitate heterogenous ammonia oxidation with molecular complexes, we have functionalized the *β*-diketiminate ligand framework enabling it to be anchored on graphitic surfaces without altering the intrinsic electronic properties of the Cu active center, following a supramolecular strategy similar to the one previously reported for related redox catalysts.[39,51–54]

In this work, we describe the preparation of a family of *β*-diketiminate ligands, shown in Chart 1, and their corresponding Cu complexes (Scheme 2). We further investigate their electrochemical and electrocatalytic properties both in homogeneous phase and when anchored on carbon fiber paper (**C$_{FP}$**) electrodes, evaluating them as heterogeneous ammonia oxidation catalysts.

RESULTS AND DISCUSSION

Synthesis of β-Diketiminate Ligands

The general strategy for preparing *β*-diketiminate ligands is outlined in Scheme 1. It involves the reaction between the *β*-diketone with the corresponding amine (for detailed procedures, see SI). Using this approach, we have synthesized several ligands, with their structures displayed in Chart 1.

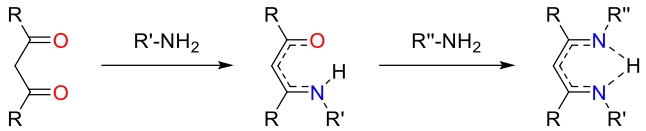

Scheme 1. General synthetic strategy for the preparation of *β*-diketiminate **HLX** (X = 1-9) ligands. Typical conditions: HCl, absolute EtOH, reflux, overnight (for R = Me); $TiCl_4$, anhydrous toluene, reflux, overnight (for R = CF_3).

These ligands were designed with some modifications to the original ligand **HL2**,[27] to investigate the roles of the CF_3 and isopropyl groups. Specifically, the exploration aimed to determine whether CF_3 groups were essential for catalysis or if they could be replaced by Me groups to potentially lower the overpotential for ammonia oxidation. Additionally, the necessity of isopropyl groups for ensuring mono-chelation was examined, as their removal could optimize the geometry of the complexes to facilitate immobilization onto the surface of the electrodes. Moreover, aromatic moieties such as biphenyl or triphenyl groups were incorporated to promote immobilization onto graphitic electrodes via CH-π and π-π interactions.

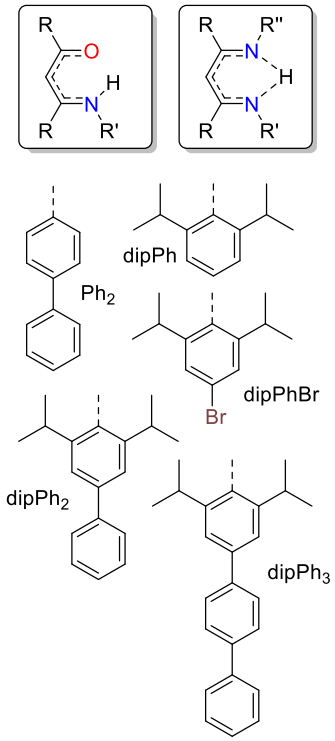

Ligand, HLX	R	R'	R''
HL1	Me	dipPh	dipPh
HL2	CF_3	dipPh	dipPh
HL3	Me	Ph_2	Ph_2
HL4	CF_3	Ph_2	Ph_2
HL5	CF_3	$dipPh_2$	$dipPh_2$
HL6	CF_3	$dipPh_3$	none*
HL7	CF_3	$dipPh_3$	$dipPh_3$
HL8	CF_3	$dipPh_3$	dipPh
HL9	Me	dipPhBr	dipPhBr
HL10	Me	$dipPh_3$	$dipPh_3$

Chart 1. Ligands (**HLX**) described in this work. Abbreviations: Ph_2, 4-biphenyl; dipPh, 1,3-diisopropylbenzene; $dipPh_2$, 2,6-diisopropylbenzene-4-phenyl; $dipPh_3$, 2,6-diisopropylbenzene-4-biphenyl; dipPhBr, 5-bromo-1,3-diisopropylbenzene. ***HL6** is a *β*-ketoiminate ligand with just one substituent at the N atom.

The non-fluorinated ligands **HL1**, **HL3** and **HL9** were prepared through the acid-catalyzed double condensation of acetylacetone.[55–61] Although **HL3** was already known in the literature,[61] we developed a new synthetic procedure, and its SC-XRD structure was resolved for the first time (Figure S104).

The **HL10** ligand, containing a triphenyl moiety, was synthesized through a Suzuki coupling between **HL9** and 4-biphenylboronic acid, since the corresponding anilinium chloride from **3** (3,5-diisopropyl-[1,1':4',1"-terphenyl]-4-amine) was insufficiently soluble for the direct double

condensation approach (see SI). This synthetic strategy, described here for the first time for *β*-diketiminate-type ligands, offers a straightforward method for preparing a wide variety of substituted ligands.

The fluorinated ligands **HL2**, **HL4**, **HL5**, **HL6**, **HL7**, and **HL8** were prepared using titanium tetrachloride as a Lewis acid to activate the aromatic amine, forming an equilibrium of highly reactive Ti complexes that react with the low-boiling point hexafluoroacetylacetone.[62–68] Notably, changing the molar ratio between hexafluoroacetylacetone, $TiCl_4$, and aniline **3** from 1.0/2.1/6.0 to 1.0/4.2/12.0 enabled the formation of either the monosubstituted *β*-ketoiminate ligand **HL6** or the disubstituted diketiminate **HL7** ligand, respectively (see SI). **HL6** can be then used as a synthetic intermediate to prepare non-symmetric fluorinated ligands such as **HL8**, which contains dipPh and $dipPh_3$ substituents, representing the first example of its kind (see Figure 1a for SC-XRD structure).

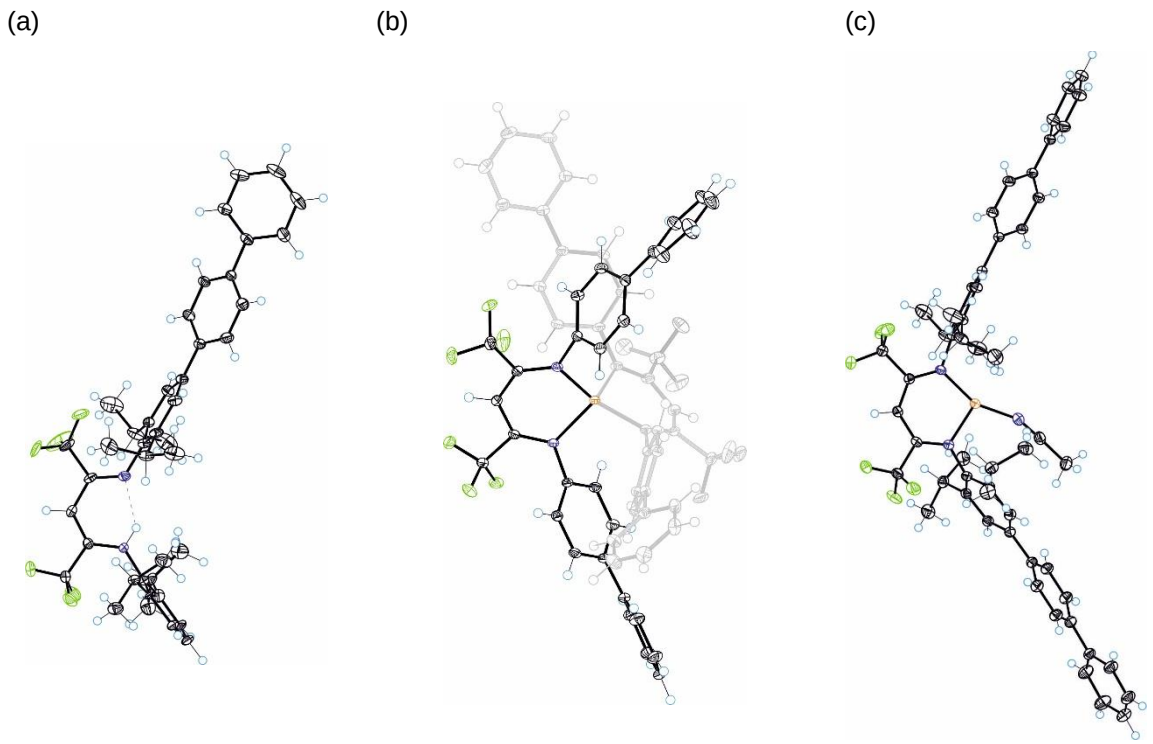

Figure 1. Solid-state structures with thermal ellipsoids at 50% probability of representative compounds prepared in this work: (a) **HL8**, (b) **[Cu^{II}(L4)$_2$]**, and (c) **[Cu^{I}(L7)(MeCN)]**. Color code: C, black; N, dark blue, H, light blue; F, green; Cu, orange. In (b) one of the two **L4** ligands is drawn in gray for better visualization of the molecular structure.

All the *β*-diketiminate ligands were purified by trituration, recrystallization, and/or column chromatography using triethylamine-deactivated silica gel (see SI for additional details). The newly synthesized ligands were characterized using standard analytical and spectroscopic techniques, including NMR, elemental analysis, and SC-XRD.

Synthesis of β-Diketiminate Cu Complexes

Scheme 2 provides a general overview of the synthesis of the Cu(I) and Cu(II) *β*-diketiminate complexes prepared in this work, which were subsequently evaluated as catalysts for ammonia oxidation. Cu^{II}(AcO)$_2$ was used as the starting material for the preparation of non-fluorinated

[Cu^{II}(LX)(AcO)] (X = 1 and 3) complexes, employing a 1:1 Cu:**HLX** stoichiometry.[69] Under the same conditions, and after screening various Cu(II) precursors and bases, the fluorinated *β*-diketiminate ligand **HL2** failed to form the corresponding Cu(II) complex due to the reduced coordination ability of the ligand in the presence of the highly electron-withdrawing CF_3 groups.

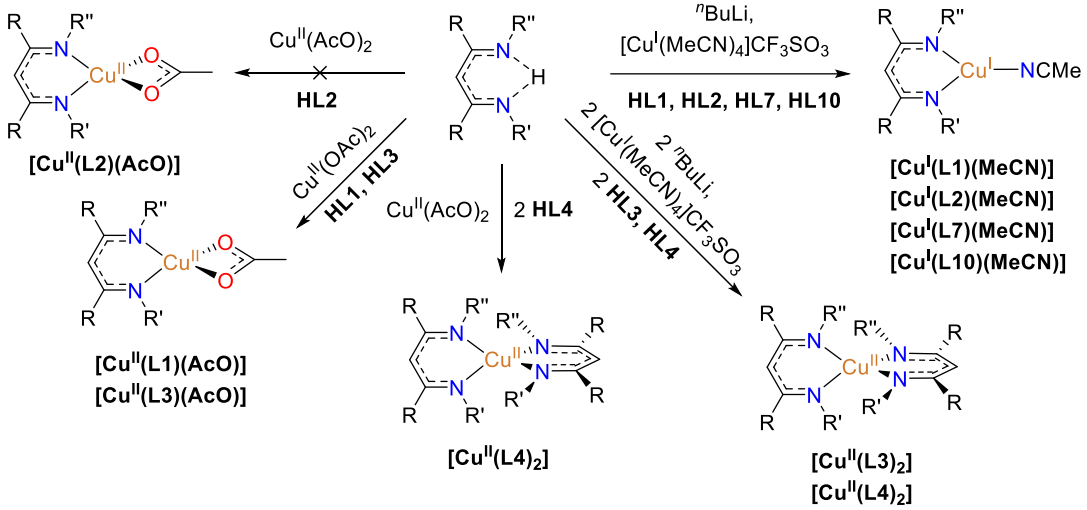

Scheme 2. Synthetic strategies for the preparation of *β*-diketiminate Cu-**LX** complexes. The **LX** ligands are described in Chart 1.

On the other hand, bis-chelated complexes **[Cu^{II}(LX)$_2$]** (X = 3 and 4) were obtained with ligands **HL3** and **HL4**, resulting in structures similar to those reported for Ni(II) complexes.[61] Complex **[Cu^{II}(L4)$_2$]** could also be synthesized starting from [Cu^I(MeCN)$_4$]CF$_3$SO$_3$, followed by disproportionation as outlined in Equation 5, a process previously described for related complexes.[70]

2 **[Cu^I(L4)(MeCN)]** → Cu^0 + **[Cu^{II}(L4)$_2$]** + 2 MeCN (5)

Sufficiently good single crystals were obtained for this complex, and its SC-XRD structure is displayed in Figure 1b, showing a pseudotetrahedral geometry for the Cu(II) metal center. Similarly, **[Cu^{II}(L3)$_2$]** was also obtained via the disproportionation route, and its SC-XRD structure is reported in the SI (Figure S112).

The [Cu^{I}(MeCN)$_4$]CF$_3$SO$_3$ complex was also used as the starting material for the preparation of **[Cu^{I}(LX)(MeCN)]** (X = 1, 2, 7 and 10) complexes, which contain sufficiently sterically hindered ligands to prevent the disproportionation reaction. An ORTEP plot of the crystal structure of **[Cu^{I}(L7)(MeCN)]** is presented in Figure 1c, showing the typical T-shape tricoordination of the Cu(I) center,[27] which is bonded to the anionic **L7**$^{-}$ ligand in a chelate manner and completed with the coordination of a monodentate MeCN ligand. To our knowledge, this is the first time that these one-pot conditions have been employed for the preparation of fluorinated *β*-diketiminate Cu(I) complexes, including the previously reported **[Cu^{I}(L2)(MeCN)]**,[27,64] with an obtained yield of 29% (see SI). In contrast, a three-step process was used in the literature to prepare **[Cu^{I}(L2)(MeCN)]** from **HL2** (Scheme 3a) with an overall yield of 66%.[27,63] Alternatively, **[Cu^{I}(L2)(MeCN)]** was synthesized in one step from **HL2** with a 76% yield,[64] using [Cu^{I}(CH$_2$SiMe$_3$)]$_4$ as a synthetic precursor (Scheme 3b).

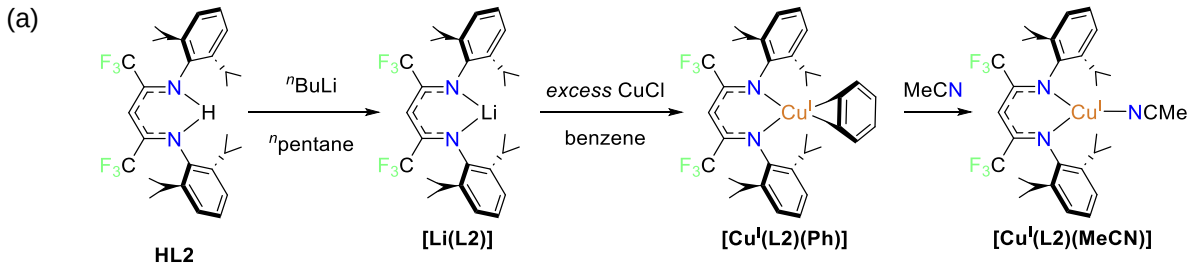

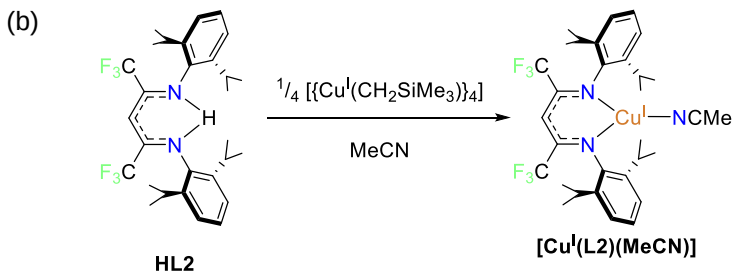

Scheme 3. Reported synthetic strategies for the preparation of **[Cu^{I}(L2)(MeCN)]**.[27,63,64]

Electrochemical Properties of the Cu-LX Complexes in Homogeneous Phase

The electrochemical properties of the complexes described in this work were investigated using cyclic voltammetry (CV) in THF and/or MeCN, with a 1 mM concentration of the complex and 100 mM $TBAPF_6$ as the supporting electrolyte. The measurements were performed with a glassy carbon disk, GC_{disk}, ($S = 0.07$ cm^2) as the working electrode (WE), a Pt disk as the counter electrode (CE), and a Ag/AgCl wire as the pseudo-reference electrode (pseudo-RE). The ferrocene $Fc^{+/0}$ redox couple served as an internal reference.

For the **[Cu^{I}(LX)(MeCN)]** (X = 1, 2, 7 and 10) complexes, a chemically reversible and electrochemically quasi-reversible wave was observed, attributed to the $Cu^{II/I}$ redox couple (Figure 2a and SI). In the case of **[Cu^{I}(L1)(MeCN)]**, this wave appears at -0.13 V vs $Fc^{+/0}$ in THF and it is shifted to +0.31 V vs $Fc^{+/0}$ (ΔE = 440 mV) with respect to **[Cu^{I}(L2)(MeCN)]**, due to the electron-withdrawing effect of the CF_3 groups. On the other hand, the triphenyl **[Cu^{I}(L7)(MeCN)]** and **[Cu^{I}(L10)(MeCN)]** complexes show slightly higher half-wave potentials compared to **[Cu^{I}(L1)(MeCN)]** and **[Cu^{I}(L2)(MeCN)]**, respectively, likely due to the larger electron delocalization of the ligands, which contain four additional aromatic rings (see Figure S100 for comparison).

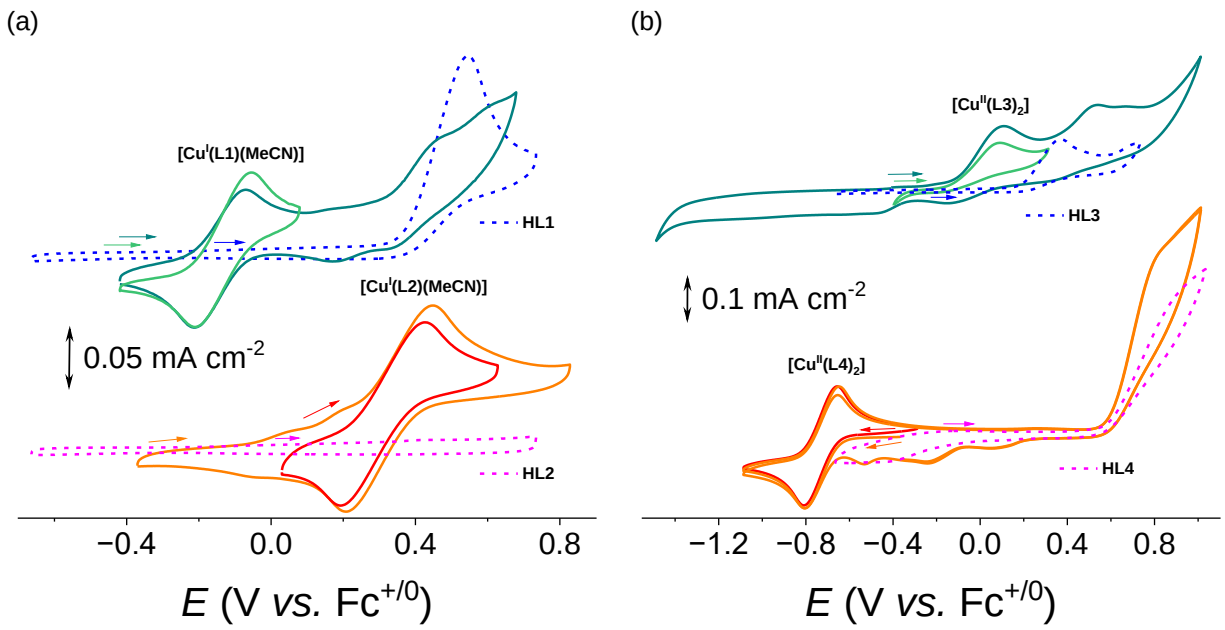

Figure 2. (a) Cyclic voltammograms in THF (μ = 0.1 M $TBAPF_6$) of non-fluorinated **[Cu^{I}(L1)(MeCN)]** (light/dark green solid lines) and fluorinated **[Cu^{I}(L2)(MeCN)]** (red/orange solid lines) complexes and their free ligands **HL1** (dashed blue line) and **HL2** (dashed pink line) under an inert atmosphere. (b) Cyclic voltammograms in THF (μ = 0.1 M $TBAPF_6$) of non-fluorinated **[Cu^{II}(L3)$_2$]** (light/dark green solid lines) and fluorinated **[Cu^{II}(L4)$_2$]** (red/orange solid lines) complexes and their respective free ligands **HL3** (dashed blue line) and **HL4** (dashed pink line) under air. *Conditions*: 1 mM concentration, GC_{disk} (S = 0.07 cm^2), WE; Pt disk, CE; Ag/AgCl wire, pseudo-RE; ν = 100 mV s^{-1}.

It is also important to note that applying potentials above and below the Cu$^{II/I}$ couple (dark green and orange CVs in Figure 2a) leads to ill-defined, chemically irreversible processes for both **[Cu^{I}(L1)(MeCN)]** and **[Cu^{I}(L2)(MeCN)]** complexes, respectively. This indicates the high reactivity of these complexes when operating beyond the Cu(II)/Cu(I) redox species. In the case of **[Cu^{I}(L1)(MeCN)]**, an irreversible process can be observed around +0.4 V vs Fc$^{+/0}$ (dark green

CV), which may be associated with ligand oxidation, as compared with the CV of the free ligand **HL1** shown in Figure 2a (blue dashed line).

The electrochemistry of the bischelated **[Cu^{II}(LX)$_2$]** (X = 3 and 4) complexes is shown in Figure 2b. For **[Cu^{II}(L4)$_2$]**, a chemically reversible and electrochemically irreversible wave is observed at -0.73 V vs $Fc^{+/0}$ (ΔE_p = 151 mV), associated with the $Cu^{II/I}$ couple (OCP = -0.54 V vs $Fc^{+/0}$). This wave is expected to appear at lower potentials for the more electron-rich **[Cu^{II}(L3)$_2$]** (OCP = -0.39 V vs $Fc^{+/0}$), although the absence of this wave is due to limitations of the solvent potential window. In contrast, at higher anodic potentials, only chemically irreversible processes are observed. For the case of **[Cu^{II}(L3)$_2$]**, a prominent chemically irreversible wave appears around 0.0 V vs $Fc^{+/0}$, while for **[Cu^{II}(L4)$_2$]**, a similar wave is observed at approximately +0.55 V vs $Fc^{+/0}$. These waves are likely due to ligand oxidation, as compared with the CVs of the free ligands **HL3** and **HL4**, shown in Figure 2b.

For the **[Cu^{II}(LX)(AcO)]** (X = 1 and 3) complexes, only chemically irreversible processes were observed, which may be associated with the loss of the acetate ligand once electron transfer processes occur (see SI).

Ammonia Oxidation Electrocatalytic Activity in Homogeneous Phase

The ammonia oxidation electrocatalytic activity of the Cu complexes described in this work was investigated using CV in THF and/or MeCN with a 1 mM concentration of the Cu complex, 100 mM $TBAPF_6$ as supporting electrolyte, a GC_{disk} (S = 0.07 cm^2) as the WE, a Pt disk as the CE and a Ag/AgCl wire as the pseudo-RE. Commercially available 0.5 M NH_3 solution in THF (Acros Organics) or self-prepared NH_3 solutions were used (see SI for preparation details). The $Fc^{+/0}$ couple served as the internal reference.

Our primary focus was to investigate the behavior of complexes **[Cu^{I}(LX)(MeCN)]** (X = 1, 2) in the presence of ammonia, and the results are presented in Figures 3-5, Scheme 4 and in the SI.

We have also tested the behavior of the other complexes in the presence of ammonia, with the results described in the SI. Additionally, we investigated the redox properties of $[Cu^{I}(MeCN)_4]^+$ under the same conditions, given the coordination properties of ammonia as monodentate ligand and the general lability of Cu(I) complexes. The results obtained are reported in Figure 3, Scheme 4 and in the SI (Figures S50-S51).

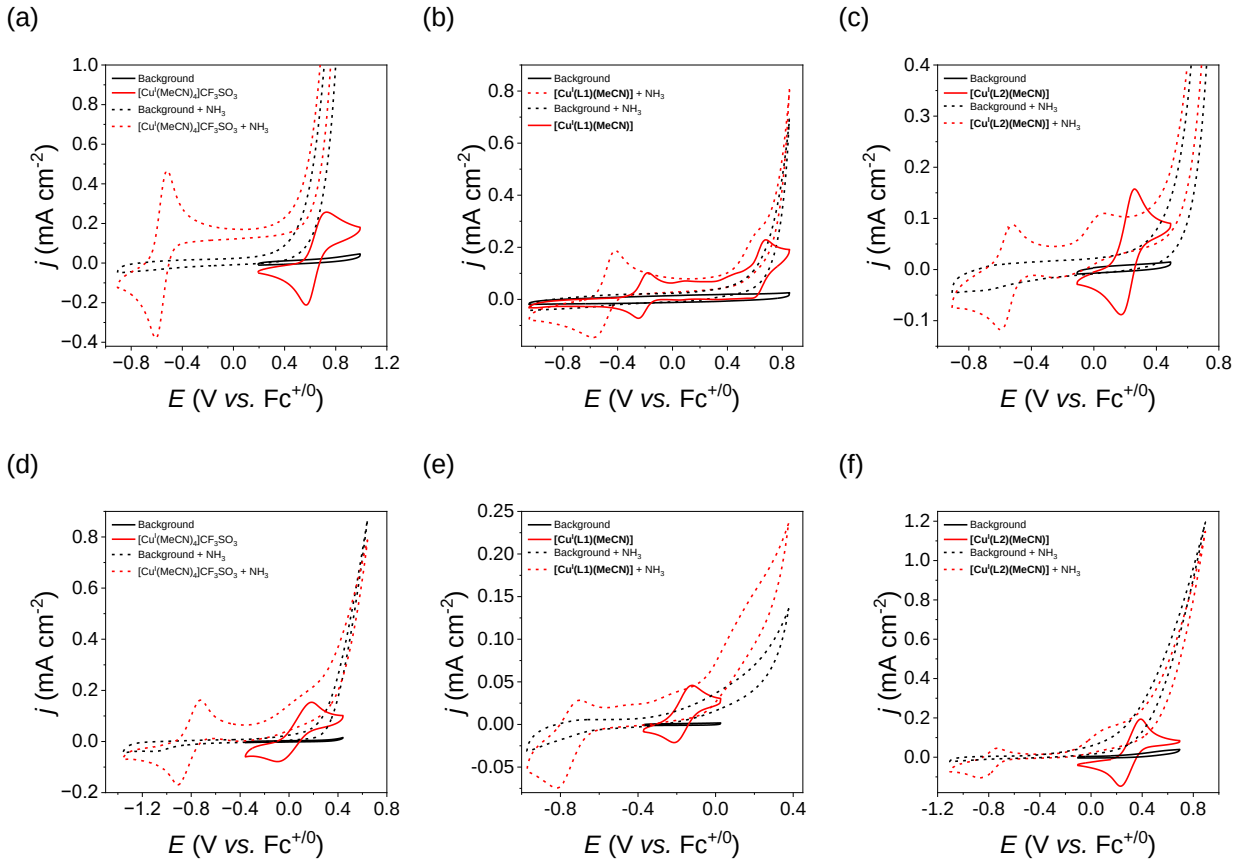

Figure 3. Cyclic voltammograms using a μ = 0.1 M $TBAPF_6$ in MeCN (top) and THF (bottom), in the absence (solid lines) and the presence (dashed lines) of 0.5 M NH_3, of $[Cu^{I}(MeCN)_4]^+$ (a and d), **[Cu^{I}(L1](MeCN)]** (b and e), and **[Cu^{I}(L2](MeCN)]** (c and f) in red lines, and the bare

electrodes in black with the same line codes. *Conditions*: under an inert atmosphere, 1 mM concentration, GC_{disk} ($S = 0.07$ cm^2), WE; Pt disk, CE; Ag/AgCl wire, pseudo-RE; $\nu = 100$ mV s^{-1}.

The $[Cu^{I}(MeCN)_4]^+$ complex in MeCN exhibits a $Cu^{II/I}$ redox couple at +0.65 V vs $Fc^{+/0}$, as shown in Figure 3a. In THF, this redox couple shifts cathodically to +0.05 V vs $Fc^{+/0}$ (Figure 3d), which is consistent with the potential formation of $[Cu^{I}(MeCN)_3]^+$ as the main species generated in THF (Scheme 4). In the presence of 0.5 M NH_3, a new wave appears at -0.57 V vs $Fc^{+/0}$, representing a 1.2 V cathodic shift in MeCN, which is associated with the formation of $[Cu^{I}(NH_3)_4]^+$. Similarly, in THF, this redox wave is further shifted to -0.80 V vs $Fc^{+/0}$ (Figure 3d). Upon scanning anodically in the presence of 0.5 M NH_3 (Figures 3a and 3d, dashed red lines), a large current emerges at approximately +0.4 V vs $Fc^{+/0}$, which is attributed to the oxidation of ammonia by the bare electrode, since it coincides closely with the current densities observed in the blank experiments (Figures 3a and 3d, dashed black lines).

A similar experiment was conducted with the non-fluorinated **[Cu^{I}(L1)(MeCN)]** complex. As seen in Figures 3b and 3e, the $Cu^{II/I}$ redox couple appears at -0.17 V vs $Fc^{+/0}$ in MeCN and at -0.13 V vs $Fc^{+/0}$ in THF, indicating that the main species remains the same in both solvents. However, upon addition of 0.5 M NH_3 new waves appear at -0.56 V vs $Fc^{+/0}$ in MeCN and at -0.81 V vs $Fc^{+/0}$ in THF, which coincide with the waves observed for the $[Cu^{I}(MeCN)_4]^+$ complex in 0.5 M NH_3. This observation suggests the existence of an equilibrium that involves the loss of the **L1**$^-$ ligand, as described in Equation 6.

$$\textbf{[Cu}^{\textbf{I}}\textbf{(L1)(MeCN)]} + 4\ NH_3 \rightleftharpoons [Cu^{I}(NH_3)_4]^+ + \textbf{L1}^- + MeCN \qquad (6)$$

The loss of the *β*-diketiminate ligand is further supported by the large cathodic shift of 390 mV and 660 mV in MeCN and THF, respectively. Continuing the anodic scan in MeCN (Figure 3b), the current obtained aligns with that of the blank. In contrast, in THF, a significant current emerges at -0.1 V vs $Fc^{+/0}$, which is attributed to the catalytic activity of **[Cu^{I}(L1)(NH$_3$)]** species (Equation 7).

$$[Cu^{I}(NH_3)_4]^+ + \mathbf{L1^-} \rightleftharpoons \mathbf{[Cu^{I}(L1)(NH_3)]} + 3\ NH_3 \quad (7)$$

This observation is consistent with previous findings where a similar species, **[Cu^{I}(L2)(NH$_3$)]**, was proposed as the active catalyst for ammonia oxidation to nitrogen, which is reflected by the anodic wave at 0.0 V vs $Fc^{+/0}$ in MeCN (Figure 3c).[27] For the **[Cu^{I}(L2)(MeCN)]** complex, a reversible wave appears at +0.22 V vs $Fc^{+/0}$ in MeCN and at +0.31 V vs $Fc^{+/0}$ in THF. As with **[Cu^{I}(L1)(MeCN)]**, the presence of 0.5 M NH_3 induces similar equilibria as described in Equations 6-7, with clear waves associated with $[Cu^{I}(NH_3)_4]^+$ formation. In this case, though, no fast catalytic currents are observed in either MeCN or THF (Figures 3c and 3f), suggesting a higher shift towards catalytically unactive $[Cu^{I}(NH_3)_4]^+$ complex. Finally, it is noteworthy that the $Cu^{II/I}$ wave for **[Cu^{I}(L2)(MeCN)]** in MeCN shifts anodically by 110 mV when measured in THF, indicating a solvation effect. Thus, the equilibria shown in Equations 6 and 7 for the **[Cu^{I}(L1)(MeCN)]** complex also applies to the complex containing the fluorinated **L2$^-$** ligand, as illustrated in Equations 8 and 9.

$$\mathbf{[Cu^{I}(L2)(MeCN)]} + NH_3 \rightleftharpoons \mathbf{[Cu^{I}(L2)(NH_3)]} + MeCN \quad (8)$$

$$\mathbf{[Cu^{I}(L2)(NH_3)]} + 3\ NH_3 \rightleftharpoons [Cu^{I}(NH_3)_4]^+ + \mathbf{L2^-} \quad (9)$$

This was corroborated by adding varying amounts of deprotonated ligand, in the form of **Li1** or **LiL2**, to the initial solutions of **[Cu^{I}(L1)(MeCN)]** and **[Cu^{I}(L2)(MeCN)]** in MeCN with 0.5 M NH_3, respectively, to shift the equilibrium towards $[Cu^{I}(NH_3)_4]^+$ consumption. As shown in Figure 4, as the amount of free ligand increases, the wave at -0.56 V vs $Fc^{+/0}$ associated with the $[Cu^{I}(NH_3)_4]^+$ complex diminishes in accordance with Le Châtelier's principle. In all cases, no catalytic activity is observed for both **[Cu^{I}(L1)(NH$_3$)]** and **[Cu^{I}(L2)(NH$_3$)]** species under these conditions.

(a) (b)

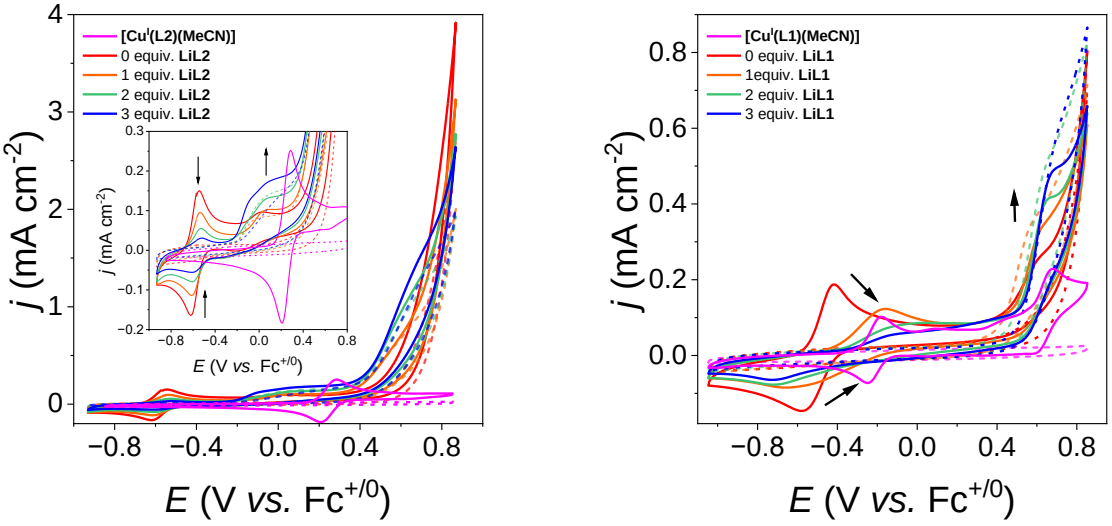

Figure 4. (a) Cyclic voltammograms of 1 mM **[Cu^{I}(L2)(MeCN)]** in MeCN (μ = 0.1 M $TBAPF_6$) containing 0.5 M NH_3 and different equivalents (0-3) of **LiL2** (solid lines), overlaid with cyclic voltammograms of **LiL2** alone as blanks (dashed lines). The pink trace corresponds to 1 mM **[Cu^{I}(L2)(MeCN)]** under identical conditions in the absence of both NH_3 and **LiL2** added. (b) Analogous data for **[Cu^{I}(L1)(MeCN)]**, using the same color code.

Further evidence for the presence of these equilibria is based on spectroscopic UV-Vis and NMR experiments that are reported in Figures S101 and S102 respectively in the SI. The wave at -0.6 V

in the CV is thus consistent with the equilibrium process indicated in Equation 9, being very fast and thus showing a complete conversion to $[Cu^{I}(NH_3)_4]^+$.

Altogether, Scheme 4 summarizes the equilibria involving complexes containing both **L1** and **L2** ligands. We anticipate that this improved understanding of ligand dissociation pathways in Cu *β*-diketiminate complexes for ammonia oxidation catalysis will enable the rational design of improved catalysts in future studies.

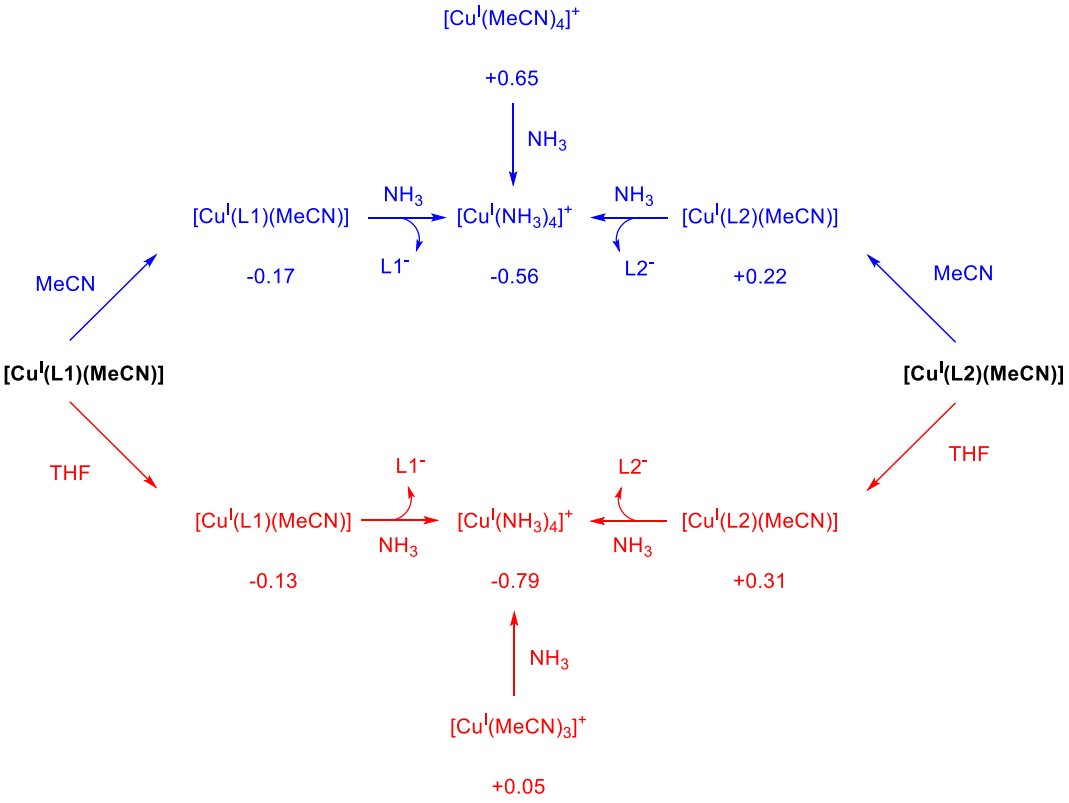

Scheme 4. Reaction scheme for $[Cu^{I}(MeCN)_4]^+$, **$[Cu^{I}$(L1)(MeCN)]**, and **$[Cu^{I}$(L2)(MeCN)]** complexes in MeCN (blue) and in THF (red) in the presence and absence of 0.5 M NH_3, based on electrochemical data. Redox potentials for the $Cu^{II/I}$ couple are given in V vs $Fc^{+/0}$ and are indicated below each species. For the $[Cu^{II/I}(NH_3)_4]^+$ couple, the values shown represent the average obtained from the three different synthetic strategies (see Figure 3).

The electrocatalytic activity of **[Cu^{I}(L1)(NH$_3$)]** species in THF was further investigated by multiple CV cycles within different potential ranges, with the results shown in Figure 5. As seen in Figure 5a, within the potential range from -0.3 V to +0.1 V vs $Fc^{+/0}$, a catalytic wave with a foot at -0.1 V vs $Fc^{+/0}$ begins to emerge. After 100 cycles, the catalytic activity decreases gradually, losing about 50% of the initial current. This is indicative of progressive catalyst degradation within the double layer. When a broader potential range up to 0.9 V vs $Fc^{+/0}$ is used (Figure 5b), large currents are observed, which could indicate some catalytic activity. However, the current densities obtained from the blank (Figures 5a and 5b; dashed black line), associated with ammonia oxidation by the bare electrode, reach values of about 50% of the observed current. Nevertheless, we have carried out a bulk electrolysis for **[Cu^{I}(L1)(NH$_3$)]** species in THF at E_{app} = 0.63 V vs $Fc^{+/0}$ and we have managed to detect a limited amount of N_2 (Figures S64-S66).

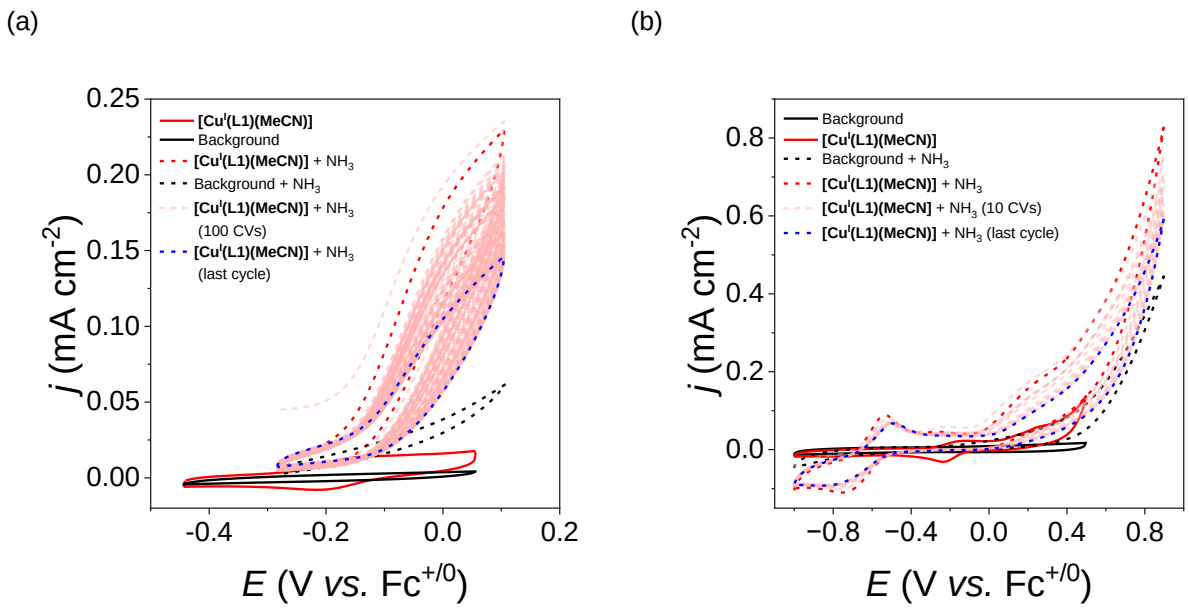

Figure 5. Cyclic voltammograms in THF (μ = 0.1 M $TBAPF_6$) of 1 mM **[Cu^{I}(L1)(MeCN)]** at different potential windows (a and b), in the absence (solid red line) and in the presence (dashed red line) of 0.5 M NH_3. The bare electrode is shown under the same conditions in the absence (solid black line) and the presence (dashed black line) of 0.5 M NH_3. *Conditions*: under an inert atmosphere, GC_{disk} (S = 0.07 cm^2), WE; Pt disk, CE; Ag/AgCl wire, pseudo-RE; ν = 100 mV s^{-1}.

The remaining complexes prepared in this work were also investigated by CV in THF and/or MeCN in the presence and absence of 0.5 M NH_3. However, none of these complexes exhibited clear catalytic activity (see SI). Nonetheless, all of them, including $Cu^{II}(AcO)_2$ as a control experiment, displayed a quasi-reversible wave around -0.7 V vs $Fc^{+/0}$ in THF in the presence of 500 equivalents of NH_3 (see Figures S49 and S52-S56). This behavior highlights the ability of NH_3 to compete for the first coordination sphere of the Cu center, resulting in the formation of the $[Cu^{II/I}(NH_3)_4]^+$ species in all cases.

Anchoring via CH-π and π-π Interactions and Heterogeneous Electrocatalytic Ammonia Oxidation

Supramolecular anchoring via CH-π and π-π interactions provides an exceptionally simple and effective method to immobilize redox catalysts, as previously demonstrated by our group for both water oxidation and CO_2 reduction catalysts.[44,48,50]

To explore this approach, we synthesized *β*-diketiminate ligands featuring additional aromatic units capable of providing supramolecular interactions with a graphitic surface, leading to the first example of heterogeneous ammonia oxidation using first-row transition metals. Figure 6 represents a DFT model for these interactions with **[Cu^{I}(L7)(MeCN)]** and **[Cu^{I}(L10)(MeCN)]** complexes. In these complexes, the triphenyl moiety facilitates up to 8 aromatic CH-π interactions (from the biphenyl group) and 8 aliphatic CH-π interactions (from the isopropyl groups), in addition to π-π interactions with the graphene surface, as shown by the red cloud representation (Figure 6). For the **[Cu^{I}(L7)(MeCN)]** complex, the anchoring energy between the molecule and the surface in THF is 67.3 kcal mol^{-1} when considering only CH-π interactions, increasing to 101.6 kcal/mol when accounting for the optimal geometry for π-π interactions (Table S4).

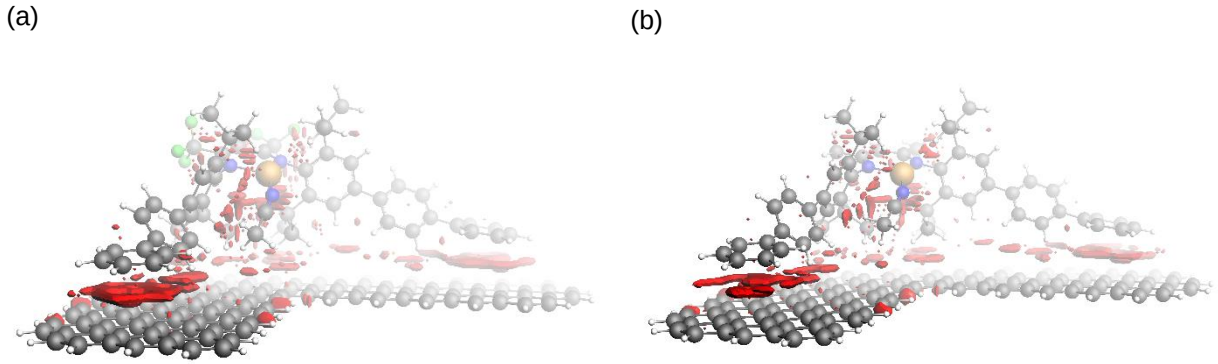

Figure 6. Optimized structures of (a) **[Cu^{I}(L7)(MeCN)]** and (b) **[Cu^{I}(L10)(MeCN)]** anchored onto a graphene layer via CH-π and π-π interactions. The supramolecular interactions are depicted

in red (more details provided in the Non-Covalent Interactions section of the SI). Color code: Gray (C), blue (N), white (H), green (F), orange (Cu).

We utilized **C$_{FP}$** electrodes, a highly porous graphitic material, as a support for immobilizing the complex **[Cu^{I}(L7)(MeCN)]**. Functionalization of the electrode was carried out under an inert atmosphere by either dipping the C_{FP} into a 0.5-1 mM solution of **[Cu^{I}(L7)(MeCN)]** in THF or MeCN for specific immersion times, or by drop-casting the solution directly onto the electrode surface (see SI for detailed protocols and conditions). The resulting molecular hybrid material, labelled as **[Cu^{I}(L7)(MeCN)]@C$_{FP}$**, was rinsed and/or used directly as the WE to evaluate its capacity for heterogeneous electrocatalytic ammonia oxidation in MeOH or TFE. Catalyst loadings onto the electrode, obtained via the dipping method, were typically ranged from 0.2-1.2 nmol cm^{-2}, reflecting a balance between the complex' surface affinity and its solubility in the solvent used. These values were estimated in MeOH from the integrated charge of the irreversible oxidative wave, assuming a one-electron transfer process (see Figure S87 for calculation details).

Figure 7a displays the CV of the **[Cu^{I}(L7)(MeCN)]@C$_{FP}$** (Γ = 1.2 nmol cm^{-2}; 0.25 cm^2) electrode in MeOH using 0.1 M $TBAPF_6$ as the supporting electrolyte. In the potential range from 0.0 to 0.2 V vs $Fc^{+/0}$, a cathodic wave appears, associated with the $Cu^{II/I}$ redox couple, the same process observed at -0.17 V vs $Fc^{+/0}$ in homogeneous phase for **[Cu^{I}(L7)(MeCN)]** in MeCN. The presence of 0.4 M NH_3 to the solution generates an electrocatalytic wave that reaches 0.66 mA cm^{-2} at +0.3 V vs $Fc^{+/0}$ (background subtracted), as seen in the figure. A controlled potential electrolysis (CPE) at E_{app} = 0.24 V vs $Fc^{+/0}$ was performed for the same electrode, and the *j* vs. t plot is shown in Figure 7b (red line), together with the blank for the bare electrode (black line). A total of $8.7 \cdot 10^{-2}$ C (blank subtracted) were passed for **[Cu^{I}(L7)(MeCN)]@C$_{FP}$**, corresponding to

$9.0 \cdot 10^{-9}$ mol of electrons, which would imply 520 turnover numbers (TONs), assuming 100% faradaic efficiency (FE) for N_2 generation (see SI for calculations). A CV of the electrode after the CPE (Figure S87a) shows approximately 76% less electrocatalytic current density (0.16 mA cm^{-2} at +0.3 V vs $Fc^{+/0}$) compared to the initial stage, due to mass loss of the catalyst from the electrode, most likely caused by the solubility of the potential intermediates generated during the process and ligand loss associated with the equilibrium indicated in Equation 9. The low stability of the anchored species during catalysis, along with the small amount of catalyst anchored on the electrode surface, hindered a quantitative analysis of the products generated during catalysis after several trials.

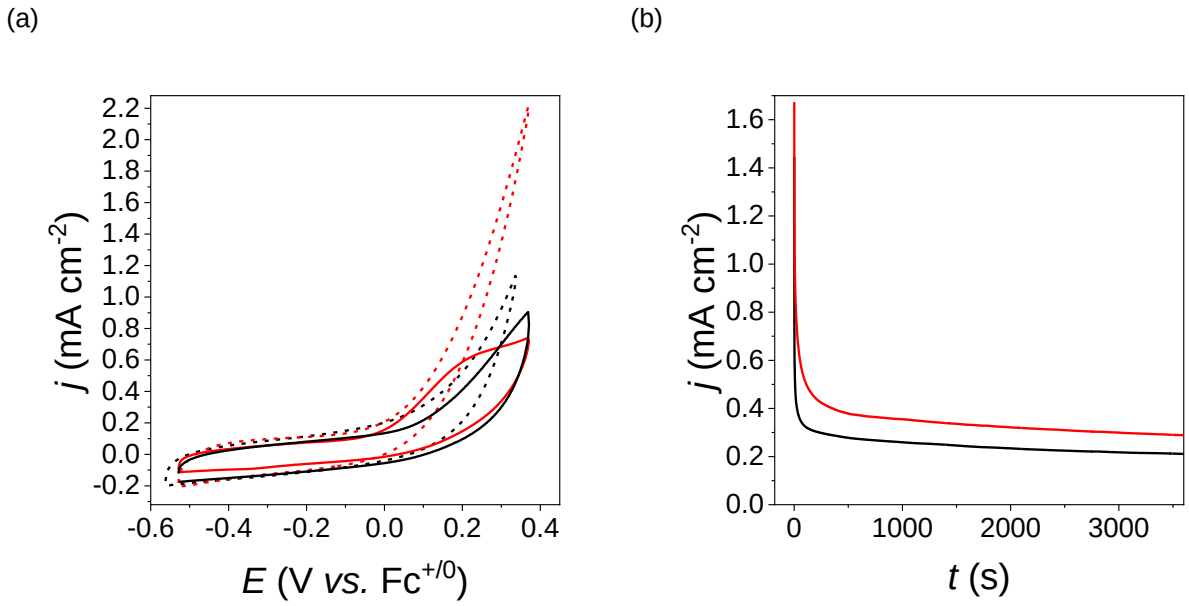

Figure 7. (a) Cyclic voltammograms in MeOH (μ = 0.1 M $TBAPF_6$) of **[Cu^{I}(L7)(MeCN)]@C_{FP}** (S = 0.25 cm^2; Γ = 1.2 nmol cm^{-2}) in the absence (solid red line) and in the presence (dashed red line) of 0.4 M NH_3. The bare electrode is shown under the same conditions in the absence (solid black line) and in the presence (dashed black line) of 0.4 M NH_3. *Conditions*: under an inert atmosphere, Pt disk, CE; Ag/AgCl wire, pseudo-RE; ν = 100 mV s^{-1}. (b) CPE of the same electrode

(red line) and the bare electrode (black line) at E_{app} = 0.24 V in MeOH (μ = 0.1 M $TBAPF_6$) in the presence of 0.4 M NH_3. Background subtracted $Q_{CPE} = 8.7 \cdot 10^{-2}$ C, TON = 520 assuming 100% FE.

As a comparison, the **[Cu^{I}(L10)(MeCN)]@C$_{FP}$** electrode in MeOH shows a rapid decrease in current after cycling in the absence of NH_3, indicating its lower anchoring stability in this solvent (Figure S70). Although DFT calculations indicated similar immobilization energies for both **[Cu^{I}(L10)(MeCN)]** and **[Cu^{I}(L10)(MeCN)]** complexes (Tables S3-S6), we attribute the detachment to the higher solubility of **[Cu^{I}(L10)(MeCN)]** in that solvent.

We also attempted to perform heterogeneous electrocatalytic ammonia oxidation using **[Cu^{I}(L7)(MeCN)]@C$_{FP}$** and **[Cu^{I}(L10)(MeCN)]@C$_{FP}$** electrodes in TFE, a solvent in which both complexes are insoluble (Tables S1-S2). However, the resulting redox processes were less defined and inconsistent, preventing the extraction of meaningful trends (Figures S91-S97 and S71-S72, respectively). Moreover, a comparative study of **[Cu^{I}(L2)(MeCN)]@C$_{FP}$** and **[Cu^{I}(L7)(MeCN)]@C$_{FP}$** electrodes in TFE revealed that the additional phenyl units contribute to more distinct electrochemical waves, likely due to the increased surface loading resulting from a greater number of supramolecular interactions with the graphitic surface, as shown in Figures S96-97.

CONCLUSIONS

We have prepared and thoroughly characterized a series of β-diketiminate ligands (**LX**, X = 1-10) containing Me and CF_3 groups, along with various aromatic substituents at the nitrogen atoms. These ligands were designed to explore catalysis and immobilization for heterogeneous ammonia

oxidation. Additionally, we synthesized a non-symmetric fluorinated *β*-diketiminate ligand, **HL8**, by isolating a *β*-ketoiminate intermediate (**HL6**), which enables the stepwise addition of substituents. Furthermore, we established a novel methodology for introducing new moieties into brominated *β*-diketiminate ligands based on Suzuki coupling. The Cu complexes of several *β*-diketiminate ligands were synthesized and characterized, and their redox properties were studied using CV and CPE electrochemical techniques. In the presence of 0.5 M NH_3, both non-fluorinated **[Cu^{I}(L1)(MeCN)]** and fluorinated **[Cu^{I}(L2)(MeCN)]** complexes rapidly establish an equilibrium involving complete ligand dissociation, resulting in the formation of $[Cu^{I}(NH_3)_4]^+$, as depicted in Scheme 4. In homogeneous conditions, **[Cu^{I}(L1)(MeCN)]** demonstrated electrocatalytic activity for ammonia oxidation, whereas **[Cu^{I}(L2)(MeCN)]** was either inactive or very slow under the employed conditions, in contrast to previous literature results.[27] The **[Cu^{I}(L7)(MeCN)]** complex, containing triphenyl groups, was anchored onto C_{FP} via supramolecular CH-π and π-π interactions, resulting in the molecular hybrid material **[Cu^{I}(L7)(MeCN)]@C$_{FP}$**. This material demonstrated activity for heterogeneous electrocatalytic ammonia oxidation, achieving 520 TONs assuming 100% FE. While this work represents the first example of heterogenous ammonia electrocatalyzed oxidation using first-row transition metal complexes, several limitations of this approach must be addressed. These include low catalyst loading, the high solubility of potential reaction intermediates, and the equilibrium formation of $[Cu^{I}(NH_3)_4]^+$, which results in *β*-diketaminato ligand dissociation and compromises system stability. Therefore, to develop improved molecular hybrid materials utilizing first-row transition metal complexes, particularly Cu, it is essential to minimize or eliminate the equilibrium that leads to $[Cu^{I}(NH_3)_4]^+$ formation. This would prevent *β*-diketaminato ligand loss and mitigate catalyst deactivation, enhancing the overall stability and efficiency of the catalytic system.

EXPERIMENTAL SECTION

General Considerations

All manipulations, unless stated otherwise, were performed under a dry inert atmosphere by utilizing an MBraun glovebox and/or Schlenk techniques. All reagents were purchased from common suppliers (e.g., Sigma Aldrich, Acros Organics, abcr GmbH, TCI, Carlo Erba Reagents) and used without further purification unless otherwise noted. Full experimental details, including synthesis, characterization, and electrochemical experiments, are provided in the Supporting Information. 4-Bromo-2,6-diisopropylaniline (**1**),[71] 3,5-diisopropyl-[1,1'-biphenyl]-4-amine (**2**),[72,73] **HL1**,[59] **HL2**,[62,63] **HL3**,[61] **[Cu^{I}(L1)(MeCN)]**,[74,75] **[Cu^{II}(L1)(OAc)]**,[69] and **[Cu^{I}(L2)(MeCN)]**[27,64] have been previously reported in the literature.

*Preparation of 3,5-diisopropyl-[1,1':4',1''-terphenyl]-4-amine (**3**)*

1 (18.0 g, 70 mmol), 4-biphenylboronic acid (21.3 g, 106 mmol, 98%) and $Pd(PPh_3)_4$ (4.10 g, 3.51 mmol, 99%) were dissolved in toluene (200 mL) and EtOH (50 mL). The mixture was purged with inert gas for 30 min. Meanwhile, Na_2CO_3 (80 mL, 2 M solution in water) was also purged with inert gas for 30 min, and then added to the reaction mixture. The biphasic reaction mixture was slowly heated to reflux, during which an exothermic reaction occurred, causing the reaction mixture to turn black. The resulting mixture was maintained under reflux overnight under an inert atmosphere. After cooling to RT, this was filtered through toluene-rinsed Celite pad, and the dark organic layer was separated and dried over anhydrous Na_2SO_4. The solvent was removed under reduced pressure and a brown/purple solid was obtained as a residue, which was purified by column chromatography (silica gel, wet loading in DCM, hexane/DCM 8:2 to DCM, $R_f \sim 0.1$) and triturated in hexane to obtain pure **3** (7.55 g, 22.9 mmol, 33%) as a white solid.

*General protocol for the preparation of non-fluorinated **HL1** and **HL3** ligands*

A solution of acetylacetone (1 equiv.) and the corresponding aromatic amine (2.1 equiv.) in absolute EtOH was prepared under an inert atmosphere. Then, concentrated HCl (1.0 equiv.) was added dropwise to the solution under stirring, and the reaction mixture was then refluxed for 24 h. Upon cooling to 0 ºC, the hydrochloride salt **HLX**·HCl precipitated as a solid, which was collected by filtration, washed with cold EtOH, and dried under vacuum. To obtain the neutral β-diketiminate ligand **HLX**, the dried salt was dissolved in DCM or $CHCl_3$, and the solution was treated with an equal volume of saturated aqueous Na_2CO_3. After thorough mixing, the organic layer was separated, washed with brine, dried over anhydrous Na_2SO_4, filtered, and concentrated under reduced pressure. The resulting residue was either used directly (**HL1**, 78% yield) or purified by recrystallization from 1:1 THF/^{n}heptane (**HL3**, 36% yield).

*General protocol for the preparation of fluorinated **HL2**, **HL4**, **HL5**, and **HL7** ligands*

Under an inert atmosphere, $TiCl_4$ (6.0-12.0 equiv.) was added dropwise to a vigorously stirred solution of the corresponding aromatic amine (2.1-4.2 equiv.) in anhydrous toluene or ^{n}heptane. A dense precipitate formed immediately. The reaction mixture was stirred for 2 h at either RT or 0 ºC. Hexafluoroacetylacetone (1.0 equiv.) was then added to the reaction mixture, and in some cases, additional solvent was introduced to aid stirring. The resulting mixture was refluxed overnight under an inert atmosphere. During the reaction, the color of the solution typically changed (e.g., from orange or red to yellow or brown), and a precipitate consisting of TiO_2 and aminium chloride byproducts formed. After cooling to RT, the precipitate was removed by vacuum filtration, and the reaction flask was rinsed with ^{n}pentane or ^{n}hexane. The combined filtrate was washed with water (x 3) and brine (x 1), then dried over anhydrous $MgSO_4$ or Na_2SO_4. The solution was filtered, and the solvent was removed under reduced pressure to afford a crude orange or

yellow residue. This residue was purified by recrystallization from MeOH (**HL2**, 23% yield) or hexane (**HL4**, 68% yield; **HL5**, 1% yield), or in some cases, further purification was achieved by column chromatography (e.g., using silica gel deactivated with 3% TEA and eluted with hexane/EtOAc 9.5/0.5, **HL7**, quantitative yield).

*Preparation of **HL6***

Under an inert atmosphere, titanium tetrachloride (1.66 mL, 15.1 mmol) was added dropwise to a vigorously stirring solution of **3** (14.2 g, 43.1 mmol) in anhydrous toluene (150 mL) at 0 ºC. The reaction mixture immediately turned dark and was stirred overnight at RT. Hexafluoroacetylacetone (1.04 mL, 7.2 mmol, 98%) was then added, and the mixture was stirred for 2 h at 90 ºC. After this time, the color of the reaction mixture turned brown, and a significant amount of precipitate consisting of titanium dioxide and **P3** hydrochloride formed. A red solution was isolated by vacuum filtration, which was washed with water (x 3) and brine (x 1). The organic layer obtained was dried over anhydrous Na_2SO_4, and the solvent was removed under reduced pressure to afford a red oil. MeOH (100 mL) was added, and the mixture was stirred at RT to form a tan powder, which was isolated by vacuum filtration and washed with MeOH to yield **HL6** (2.02 g, 3.89 mmol, 54%).

*General protocol for the preparation of **HL7** and **HL8** from **HL6***

Under an inert atmosphere, $TiCl_4$ (6.0 equiv.) was added dropwise to a vigorously stirred solution of the corresponding aromatic amine (2.1 equiv.) in anhydrous toluene. A dense precipitate formed immediately, indicating coordination to the amine. The reaction mixture was stirred for 2 h at RT. After this time, a solution of **HL6** (1.0 equiv.) in anhydrous toluene was added to the reaction mixture. The resulting mixture was refluxed overnight under an inert atmosphere. During this period, the reaction mixture typically darked in color (e.g., orange to dark

brown) and a substantial precipitate formed, primarily composed of $TiCl_4$ and aminium chloride byproducts. Upon completion, the mixture was cooled to RT, and the solid byproducts were removed by vacuum filtration. The filtrate was washed sequentially with water (x 3) and brine (x 1), then dried over anhydrous Na_2SO_4. The organic phase was filtered and concentrated under reduced pressure to yield a crude solid residue. The crude residue was triturated with MeOH, affording the desired products (**HL7**, 78% yield; **HL8**, 64% yield) as a yellow solid, which was collected by filtration and dried under vacuum.

*Preparation of **HL9***

Concentrated HCl (4.6 mL, 55 mmol, 37%) was added dropwise to a solution of acetylacetone (5.8 mL, 56 mmol) and **1** (28.5 g, 111 mmol) in absolute EtOH (200 mL). The resulting mixture was refluxed overnight. After cooling the reaction mixture to RT, hydrochloride salt **HL9**·HCl formed as a white precipitate. The solvent was removed under vacuum, leaving an orange residue, which was refluxed with cyclohexane (300 mL) for 1 h. The resulting slurry was then allowed to cool to RT, filtered, and the solid was dissolved in DCM (300 mL). This solution was mixed with a saturated aqueous Na_2CO_3 solution (200 mL) and stirred until the solid dissolved. The organic layer was separated, washed with water (3 x 200 mL) and brine (200 mL), dried over anhydrous Na_2SO_4, and filtered. The solvent was removed under reduced pressure, yielding a pinkish residue, which was triturated with hexane and filtered to obtain **HL9** (10.11 g, 17.5 mmol, 31%) as a white solid.

*Preparation of **HL10***

HL9 (5.76 g, 10.0 mmol), 4-biphenylboronic acid (5.95 g, 30.0 mmol) and $Pd(PPh_3)_4$ (584 mg, 0.50 mmol) were mixed in toluene (100 mL) and EtOH (25 mL). The mixture was purged with inert gas for 30 min. Meanwhile, Na_2CO_3 (25 mL, 2 M solution in water) was also purged with

inert gas for 30 min, and then added to the reaction mixture. The biphasic reaction mixture was refluxed overnight. After cooling to RT, the mixture was filtered through a toluene-rinsed Celite pad, and the dark organic layer was separated, washed with brine, and dried over anhydrous Na_2SO_4 and filtered. The solvent was removed under reduced pressure, yielding a brown solid residue. This residue was purified by column chromatography (wet loading in eluent, silica gel deactivated with 3% TEA, DCM/hexane 8:2, R_f ~ 0.9) and triturated with hexane to afford **HL10** (5.49 g, 7.6 mmol, 76%) as a white solid.

Preparation of ***[Cu^{II}(L3)(OAc)]***

A solution of **HL3** (40 mg, 0.1 mmol) in $CHCl_3$ (5 mL) was added to a stirring MeOH (15 mL) solution of $Cu^{II}(AcO)_2$ (19 mg, 0.1 mmol, 98%). The resulting dark mixture was refluxed overnight. After this time, the solvent was removed under reduced pressure, and the residue was triturated with Et_2O (10 mL). The solid was filtered and washed with MeOH to yield **[Cu^{II}(L3)(AcO)]** (18 mg, 0.034 mmol, 34%) as a dark brown powder.

Preparation of ***[Cu^{II}(L3)$_2$]***

Inside a glovebox ([H_2O < 0.1 ppm, [O_2] < 0.1 ppm), a solution of ^{n}BuLi (2.5 M in hexanes, 0.24 mL, 0.60 mmol) was carefully added dropwise at RT to a stirring solution of **HL3** (200 mg, 0.50 mmol) in anhydrous THF (5 mL), avoiding overheating. The resulting orange mixture was stirred at RT for 3 h. After this time, $[Cu^I(MeCN)_4]CF_3SO_3$ (189 mg, 0.50 mmol) was added to the reaction mixture, turning it dark. The mixture was stirred at RT for an additional 10 min. All volatiles were then removed under dynamic vacuum, leaving a red residue that was suspended in anhydrous ^{n}pentane (3 x 20 mL) and filtered through a Celite plug. The volatiles of the filtrate were removed under dynamic vacuum, yielding a brown residue. This residue was recrystallized

from ^{n}pentane (RT/-40 ºC) to obtain **[$Cu^{II}(L3)_2$]** (37 mg, 0.042 mmol, 17%) as dark brown crystals.

Preparation of ***[$Cu^{II}(L4)_2$]***

A solution of **HL4** (102 mg, 0.1 mmol) in $CHCl_3$ (5 mL) was added to a stirring MeOH (15 mL) solution of $Cu^{II}(AcO)_2$ (19 mg, 0.1 mmol). The resulting dark mixture was refluxed overnight. After this time, the reaction mixture was left to cool to RT, and dark brown precipitates formed. The solvent of the reaction mixture was removed under reduced pressure, and the residue was triturated with MeOH (10 mL) and filtered to yield **[$Cu^{II}(L4)_2$]** (57 mg, 0.053 mmol, 53%) as a dark brown powder.

General protocol for the preparation of ***[$Cu^{I}(L1)(MeCN)$]***, ***[$Cu^{I}(L2)(MeCN)$]***, ***[$Cu^{I}(L7)(MeCN)$]***, *and* ***[$Cu^{I}(L10)(MeCN)$]*** *complexes*

Inside a glovebox ([H_2O] < 0.1 ppm, [O_2] < 0.1 ppm), a solution of ^{n}BuLi (2.5 M in hexanes, 1.0-2.0 equiv.) was carefully added dropwise at RT to a stirring solution of the corresponding **β**-diketiminate ligand **HLX** (1.0 equiv.) in anhydrous THF, avoiding overheating. The resulting mixture was stirred at RT for 3 h. After this time, $[Cu^{I}(MeCN)_4]CF_3SO_3$ (1.0 equiv.) was added to the reaction mixture, resulting in a darkening of the solution. The reaction was stirred at RT for an additional 10 min. All volatiles were then removed under dynamic vacuum, leaving behind a colored residue that was suspended in anhydrous ^{n}pentane or benzene (3 x 10-20 mL) and filtered through a Celite plug. The volatiles from the filtrate were removed under dynamic vacuum to yield a crude product. The resulting solid residue was then recrystallized from ^{n}pentane or MeCN (RT/-40 ºC), and washed with cold ^{n}pentane to afford the pure **[Cu^{I}(LX)(MeCN)]** complex as crystalline material (X = 1, 40% yield; X = 2, 29% yield; X = 7, 48% yield; X = 10, 18%).

ASSOCIATED CONTENT

Experimental protocols, electrochemical data, X-ray diffraction characterization and computational details can be found free of charge in the supporting information (PDF). CCDC 2410168-2410180 contains the supplementary crystallographic data for this paper. These data can be obtained free of charge via www.ccdc.cam.ac.uk/data_request/cif, or by emailing data_request@ccdc.cam.ac.uk, or by contacting The Cambridge Crystallographic Data Centre, 12 Union Road, Cambridge CB2 1EZ, UK; fax +44 1223 336033. Calculations are uploaded on ioChem: https://doi.org/10.19061/iochem-bd-1-363.

AUTHOR INFORMATION

Corresponding Author

Antoni Llobet – Institute of Chemical Research of Catalonia (ICIQ), Barcelona Institute of Science and Technology (BIST), 43007 Tarragona, Spain; Departament de Química, Universitat Autònoma de Barcelona, 08193 Cerdanyola del Vallès, Spain; orcid.org/0000-0002-6176-5272; Email: allobet@iciq.cat

Author Contributions

J.A.G.-O. performed the synthesis, characterization, and electrochemical experiments, and wrote the paper. M.M.-B. and J.B.-B. performed the single crystal X-ray structure determinations. C.B. designed the computational part. M.N. and M.S. performed the theoretical calculations. A.B. and X.S. supervised the project. A.L. conceived the idea of the project, supervised the project and wrote the paper. All authors have given approval to the final version of the manuscript.

Funding Sources

ACKNOWLEDGMENTS

J.A.G.-O. acknowledges Ministerio de Ciencia e Innovación (MICINN) for the PhD grant FPU21/04681 and ICIQ Research Support Area. MN acknowledges MICINN for the grant PRE2020-093521. C. B. acknowledges the Spanish Ministry of Science, Innovation and Universities MCIN/AEI/10.13039/501100011033 (PID2023-153344NB-I00, and CEX2019-000925-S), the ICIQ Foundation and the CERCA program of the Generalitat de Catalunya for funding. X.S. acknowledges MINECO/FEDER (PID2019-104171RB-I00), MICINN (PID2023-146787OB-I00) and AGAUR (2023CLIMA 00036). AL acknowledges MICINN through project PID2022-140143OB-I00, Generalitat de Catalunya for the project 2021 SGR 01583 and Severo Ochoa (CEX2019-000925-S).

ABBREVIATIONS

WE, working electrode; RE, reference electrode; CE, counter electrode; Fc, ferrocene; THF, tetrahydrofuran; TFE, 2,2,2-trifluoroethanol; $TBAPF_6$, Tetrabutylammonium hexafluorophosphate; GC, glassy carbon; C_{FP} carbon fiber paper; CPE, controlled potential electrolysis; CV, cyclic voltammetry; TON, turnover number.

REFERENCES

1 J. Schwartz, A Milestone for Carbon Dioxide in the Atmosphere, *The New York Times*, 2016.
2 R. McSeeney and A. Tandon, Mapped: How climate change affects extreme weather around the world, *Carbon Brief.* https://interactive.carbonbrief.org/attribution-studies/, (accessed November 21, 2024).
3 European Commission, *Consequences of climate change*, https://climate.ec.europa.eu/climate-change/consequences-climate-change_en, (accessed November 21, 2024).
4 World Meteorological Organization, *Extreme weather*, https://wmo.int/topics/extreme-weather, (accessed November 21, 2024).
5 C. Linares and J. Díaz, Spain and extreme weather events: the Health and Climate Observatory needs to be set up as a matter of urgency, *SMC España.* https://sciencemediacentre.es/en/spain-and-extreme-weather-events-health-and-climate-change-observatory-needs-be-set-matter-urgency, (accessed November 21, 2024).
6 SUNERGY, *SUNRISE Technological Roadmap*, https://sunergy-initiative.eu/project/sunrise-technological-roadmap/, (accessed November 21, 2024).
7 A. H. Trullo, Is ammonia the fuel of the future?, *Chemical & Engineering News*, https://cen.acs.org/business/petrochemicals/ammonia-fuel-future/99/i8, (accessed November 21, 2024).
8 K. Morita, Ammonia - a fuel of the future?, *Euractiv*, https://www.euractiv.com/section/energy-environment/opinion/ammonia-a-fuel-of-the-future/, (accessed November 21, 2024).
9 D. R. MacFarlane, P. V. Cherepanov, J. Choi, B. H. R. Suryanto, R. Y. Hodgetts, J. M. Bakker, F. M. Ferrero Vallana and A. N. Simonov, A Roadmap to the Ammonia Economy, *Joule*, 2020, **4**, 1186–1205.
10 W. I. F. David, G. D. Agnew, R. Bañares-Alcántara, J. Barth, J. B. Hansen, P. Bréquigny, M. de Joannon, S. F. Stott, C. F. Stott, A. Guati-Rojo, *et al.*, 2023 Roadmap on Ammonia as a Carbon-Free Fuel, *J. Phys. Energy*, 2024, **6**, 021501.
11 H. Tan, Z. Sang, Y. Tian, W. Peng, X. Liu and J. Liang, Ammonia as a Green Carbon-Free Fuel: A Pathway to the Sustainable Energy Economy, *ACS Energy Lett.*, 2024, **9**, 5120–5136.
12 P. L. Dunn, B. J. Cook, S. I. Johnson, A. M. Appel and R. M. Bullock, Oxidation of Ammonia with Molecular Complexes, *J. Am. Chem. Soc.*, 2020, **142**, 17845–17858.
13 Handbook of Chemistry and Physics, https://hbcp.chemnetbase.com, (accessed November 21, 2024).
14 L. Merakeb and M. Robert, Advances in Molecular Electrochemical Activation of Dinitrogen, *Curr. Opin. Electrochem.,* 2021, **29**, 100834.
15 R. Francke, B. Schille and M. Roemelt, Homogeneously Catalyzed Electroreduction of Carbon Dioxide - Methods, Mechanisms, and Catalysts, *Chem. Rev.*, 2018, **118**, 4631–4701.
16 Amogy: ammonia-powered semi-truck, *Ammonia Energy Association*, https://ammoniaenergy.org/articles/amogy-ammonia-powered-semi-truck/, (accessed November 21, 2024).
17 N. M. Adli, H. Zhang, S. Mukherjee and G. Wu, Review - Ammonia Oxidation Electrocatalysis for Hydrogen Generation and Fuel Cells, *J. Electrochem. Soc.*, 2018, **165**, J3130–J3147.
18 B. E. R. Snyder, M. L. Bols, H. M. Rhoda, D. Plessers, R. A. Schoonheydt, B. F. Sels and E. I. Solomon, Cage Effects Control the Mechanism of Methane Hydroxylation in Zeolites*, Science*, 2021, **373**, 327–331.

19 *ScienceDirect Topics*, Direct Methanol Fuel Cell, https://www.sciencedirect.com/topics/engineering/direct-methanol-fuel-cell, (accessed 21 November 2024).
20 *The Ethylene Technology Report 2016*, Research and Markets, 2016, https://www.researchandmarkets.com/ (accessed June 19, 2016).
21 H.-Y. Liu, H. M. C. Lant, C. C. Cody, J. Jelušić, R. H. Crabtree and G. W. Brudvig, Electrochemical Ammonia Oxidation with Molecular Catalysts, *ACS Catal.*, 2023, **13**, 4675–4682.
22 Z.-H. Lyu, J. Fu, T. Tang, J. Zhang and J.-S. Hu, Design of Ammonia Oxidation Electrocatalysts for Efficient Direct Ammonia Fuel Cells, *EnergyChem*, 2023, **5**, 100093.
23 H. Toda, K. Kuroki, R. Kanega, S. Kuriyama, K. Nakajima, Y. Himeda, K. Sakata and Y. Nishibayashi, Manganese-Catalyzed Ammonia Oxidation into Dinitrogen under Chemical or Electrochemical Conditions, *ChemPlusChem*, 2021, **86**, 1511–1516.
24 D. N. Stephens, R. K. Szilagyi, P. N. Roehling, N. Arulsamy and M. T. Mock, Catalytic Ammonia Oxidation to Dinitrogen by a Nickel Complex, *Angew. Chem., Int. Ed.*, 2023, **62**, e202213462.
25 S. Johnston, L. Kemp, B. Turay, A. N. Simonov, B. H. R. Suryanto and D. R. MacFarlane, Copper-Catalyzed Electrosynthesis of Nitrite and Nitrate from Ammonia: Tuning the Selectivity via an Interplay Between Homogeneous and Heterogeneous Catalysis, *ChemSusChem*, 2021, **14**, 4793–4801.
26 H.-Y. Liu, H. M. C. Lant, J. L. Troiano, G. Hu, B. Q. Mercado, R. H. Crabtree and G. W. Brudvig, Electrocatalytic, Homogeneous Ammonia Oxidation in Water to Nitrate and Nitrite with a Copper Complex, *J. Am. Chem. Soc.*, 2022, **144**, 8449–8453.
27 M. E. Ahmed, M. Raghibi Boroujeni, P. Ghosh, C. Greene, S. Kundu, J. A. Bertke and T. H. Warren, Electrocatalytic Ammonia Oxidation by a Low-Coordinate Copper Complex, *J. Am. Chem. Soc.*, 2022, **144**, 21136–21145.
28 M. D. Zott, P. Garrido-Barros and J. C. Peters, Electrocatalytic Ammonia Oxidation Mediated by a Polypyridyl Iron Catalyst, *ACS Catal.*, 2019, **9**, 10101–10108.
29 M. D. Zott and J. C. Peters, Enhanced Ammonia Oxidation Catalysis by a Low-Spin Iron Complex Featuring Cis Coordination Sites, *J. Am. Chem. Soc.*, 2021, **143**, 7612–7616.
30 Y. Li, J.-Y. Chen, Q. Miao, X. Yu, L. Feng, R.-Z. Liao, S. Ye, C.-H. Tung and W. Wang, A Parent Iron Amido Complex in Catalysis of Ammonia Oxidation, *J. Am. Chem. Soc.*, 2022, **144**, 4365–4375.
31 M. D. Zott and J. C. Peters, Improving Molecular Iron Ammonia Oxidation Electrocatalysts via Substituent Effects That Modulate Standard Potential and Stability, *ACS Catal.*, 2023, **13**, 14052–14057.
32 M. R. Boroujeni, C. Greene, J. A. Bertke, T. Cundari and T. H. Warren, Chemical and Electrocatalytic Ammonia Oxidation by Ferrocenium, *ChemRxiv*, 2023, preprint, DOI: 10.26434/chemrxiv-2023-l1dtg-v2.
33 L. Liu, S. I. Johnson, A. M. Appel and R. M. Bullock, *Angewandte Chemie International Edition*, 2024, **63**, e202402635.
34 M. E. Ahmed, R. J. Staples, T. R. Cundari and T. H. Warren, Electrocatalytic Ammonia Oxidation by Pyridyl-Substituted Ferrocenes, *J. Am. Chem. Soc.*, 2025, **147**, 6514–6522.
35 F. Habibzadeh, S. L. Miller, T. W. Hamann and M. R. Smith, Homogeneous Electrocatalytic Oxidation of Ammonia to N_2 under Mild Conditions, *Proceedings of the National Academy of Sciences*, 2019, **116**, 2849–2853.

36 P. Bhattacharya, Z. M. Heiden, G. M. Chambers, S. I. Johnson, R. M. Bullock and M. T. Mock, Catalytic Ammonia Oxidation to Dinitrogen by Hydrogen Atom Abstraction, *Angew. Chem. Int. Ed*, 2019, **58**, 11618–11624.
37 K. Nakajima, H. Toda, K. Sakata and Y. Nishibayashi, Ruthenium-Catalysed Oxidative Conversion of Ammonia into Dinitrogen, *Nat. Chem.*, 2019, **11**, 702–709.
38 P. L. Dunn, S. I. Johnson, W. Kaminsky and R. M. Bullock, Diversion of Catalytic C–N Bond Formation to Catalytic Oxidation of NH_3 through Modification of the Hydrogen Atom Abstractor, *J. Am. Chem. Soc.*, 2020, **142**, 3361–3365.
39 L. Sévery, J. Szczerbiński, M. Taskin, I. Tuncay, F. Brandalise Nunes, C. Cignarella, G. Tocci, O. Blacque, J. Osterwalder, R. Zenobi, M. Iannuzzi and S. D. Tilley, Immobilization of Molecular Catalysts on Electrode Surfaces Using Host–Guest Interactions, *Nat. Chem.*, 2021, **13**, 523–529.
40 J. Holub, N. Vereshchuk, F.-J. Sánchez-Baygual, M. Gil-Sepulcre, J. Benet-Buchholz and A. Llobet, Synthesis, Structure, and Ammonia Oxidation Catalytic Activity of Ru-NH_3 Complexes Containing Multidentate Polypyridyl Ligands, *Inorg. Chem.*, 2021, **60**, 13929–13940.
41 M. J. Trenerry, C. M. Wallen, T. R. Brown, S. V. Park and J. F. Berry, Spontaneous N_2 Formation by a Diruthenium Complex Enables Electrocatalytic and Aerobic Oxidation of Ammonia, *Nat. Chem.*, 2021, **13**, 1221–1227.
42 S. I. Jacob, A. Chakraborty, A. Chamas, R. Bock, L. Sepunaru and G. Ménard, Rapid Aqueous Ammonia Oxidation to N_2 Using a Molecular Ru Electrocatalyst, *ACS Energy Lett.*, 2023, **8**, 3760–3766.
43 G. Chen, P. He, C. Liu, X.-F. Mo, J.-J. Wei, Z.-W. Chen, T. Cheng, L.-Z. Fu and X.-Y. Yi, Direct Synthesis of Hydrazine by Efficient Electrochemical Ruthenium-Catalysed Ammonia Oxidation, *Nat Catal*, 2023, **6**, 949–958.
44 A. M. Beiler, A. Denisiuk, J. Holub, F.-J. Sánchez-Baygual, M. Gil-Sepulcre, M. Z. Ertem, D. Moonshiram, A. Piccioni and A. Llobet, Heterogeneous Electrochemical Ammonia Oxidation with a Ru-bda Oligomer Anchored on Graphitic Electrodes via CH−π Interactions, *ACS Energy Lett.*, 2023, **8**, 172–178.
45 C.-P. Chen, W. Alharbi, T. R. Cundari, T. W. Hamann and M. R. I. Smith, Deciphering the Mechanism of Base-Triggered Conversion of Ammonia to Molecular Nitrogen and Methylamine to Cyanide, *J. Am. Chem. Soc.*, 2023, **145**, 26339–26349.
46 H. Toda, R. Kanega, T. Yano, T. Yoshikawa, S. Kuriyama, Y. Himeda, K. Sakata and Y. Nishibayashi, Electrochemical Ammonia Oxidation Catalyzed by Ruthenium Complexes: Investigation of Substituent Effect of Axial Pyridine Ligands, *Chem. Lett.*, 2024, **53**, upae040.
47 D. N. Stephens and M. T. Mock, Molecular Complexes for Catalytic Ammonia Oxidation to Dinitrogen and the Cleavage of N−H Bonds, *Eur. J. Inorg. Chem.*, 2024, **27**, e202400039.
48 Z.-M. Luo, J.-W. Wang, M. Nicaso, M. Gil-Sepulcre, E. Solano, V. Nikolaou, J. Benet, M. Segado-Centellas, C. Bo and A. Llobet, Supramolecular Anchoring of Fe(III) Molecular Redox Catalysts into Graphitic Surfaces Via CH-π and π–π Interactions for CO_2 Electroreduction, *Angew. Chem. Int. Ed.*, 2024, **63**, e202412188.
49 J. B. Zimmerman, P. T. Anastas, H. C. Erythropel and W. Leitner, Designing for a Green Chemistry Future, *Science*, 2020, **367**, 397–400.
50 A. M. Beiler, W. Li, A. Denisiuk, E. Palomares and A. Llobet, Solar Hydrogen Production from Electrochemical Ammonia Splitting Powered by a Single Perovskite Solar Cell, *J. Energy Chem.*, 2024, **92**, 292–295.

51 H. Roithmeyer, L. Sévery, T. Moehl, B. Spingler, O. Blacque, T. Fox, M. Iannuzzi and S. D. Tilley, Electrocatalytic Ammonia Oxidation with a Tailored Molecular Catalyst Heterogenized via Surface Host–Guest Complexation, *J. Am. Chem. Soc.*, 2024, **146**, 430–436.
52 D. Schindler, M. Gil-Sepulcre, J. O. Lindner, V. Stepanenko, D. Moonshiram, A. Llobet and F. Würthner, Efficient Electrochemical Water Oxidation by a Trinuclear Ru(bda) Macrocycle Immobilized on Multi-Walled Carbon Nanotube Electrodes, *Adv. Energy Mater.*, 2020, **10**, 2002329.
53 M. A. Hoque, M. Gil-Sepulcre, A. de Aguirre, J. A. A. W. Elemans, D. Moonshiram, R. Matheu, Y. Shi, J. Benet-Buchholz, X. Sala, M. Malfois, E. Solano, J. Lim, A. Garzón-Manjón, C. Scheu, M. Lanza, F. Maseras, C. Gimbert-Suriñach and A. Llobet, Water Oxidation Electrocatalysis Using Ruthenium Coordination Oligomers Adsorbed on Multiwalled Carbon Nanotubes, *Nat. Chem.*, 2020, **12**, 1060–1066.
54 M. Gil-Sepulcre, J. O. Lindner, D. Schindler, L. Velasco, D. Moonshiram, O. Rüdiger, S. DeBeer, V. Stepanenko, E. Solano, F. Würthner and A. Llobet, Surface-Promoted Evolution of Ru-bda Coordination Oligomers Boosts the Efficiency of Water Oxidation Molecular Anodes, *J. Am. Chem. Soc.*, 2021, **143**, 11651–11661.
55 J. Feldman, S. J. McLain, A. Parthasarathy, W. J. Marshall, J. C. Calabrese and S. D. Arthur, Electrophilic Metal Precursors and a *β*-Diimine Ligand for Nickel(II)- and Palladium(II)-Catalyzed Ethylene Polymerization, *Organometallics*, 1997, **16**, 1514–1516.
56 W. Clegg, E. K. Cope, A. J. Edwards and F. S. Mair, Structural Characterization of [(2,6-$Pr^i_2C_6H_3$)NC(Me)C(H)C(Me)N(2,6-$Pr^i_2C_6H_3$)K·$PhCH_3$]$_\infty$: A Heavy Alkali Metal Diazapentadienyl Complex, *Inorg. Chem.*, 1998, **37**, 2317–2319.
57 M. Stender, R. J. Wright, B. E. Eichler, J. Prust, M. M. Olmstead, H. W. Roesky and P. P. Power, The Synthesis and Structure of Lithium Derivatives of the Sterically Encumbered *β*-Diketiminate Ligand [{(2,6-$Pr^i_2H_3C_6$)N(CH3)C}2CH]$^-$, and a Modified Synthesis of the Aminoimine Precursor, *J. Chem. Soc., Dalton Trans.*, 2001, 3465–3469.
58 Y.-M. Yao, Y.-J. Luo, R. Jiao, Q. Shen, K.-B. Yu and L.-H. Weng, Synthesis of Lanthanide Chlorides Supported by *β*-Diketiminate Ligands and Molecular Structures of $L^1SmCl_2(THF)_2$ and $L^2SmCl_2(THF)_2$ [L^1=PhNC(Me)CHC(Me)NPh; L^2=*p*-ClPhNC(Me)CHC(Me)NPh(2,6-Pr^i_2)], *Polyhedron*, 2003, **22**, 441–446.
59 R. B. Muterle, F. Fabri, R. Buffon, W. de Oliveira and U. Schuchardt, Synthesis of a Bis(Diketiminate)Bromosamarium(III) Complex and Its Activity in the Polymerization of Methyl Methacrylate, *Appl. Catal. A*, 2007, **317**, 149–153.
60 M. P. Crockett, A. S. Wong, B. Li and J. A. Byers, Rational Design of an Iron-Based Catalyst for Suzuki–Miyaura Cross-Couplings Involving Heteroaromatic Boronic Esters and Tertiary Alkyl Electrophiles, *Angew. Chem. Int. Ed.*, 2020, **59**, 5392–5397.
61 J. E. Parks and R. H. Holm, Synthesis, Solution Stereochemistry, and Electron Delocalization Properties of Bis(.Beta.-Iminoamino)Nickel(II) Complexes, *Inorg. Chem.*, 1968, **7**, 1408–1416.
62 D. T. Carey, E. K. Cope-Eatough, E. Vilaplana-Mafé, F. S. Mair, R. G. Pritchard, J. E. Warren and R. J. Woods, Structures and Reactions of Monomeric and Dimeric Lithium Diazapentadienyl Complexes with Electrophiles: Synthesis of α- C,C′ -Dialkyl-*β*-Diimines, and Dissolution-Reversible Synthesis of an α-Alkoxylithium-*β*-Diimine, *Dalton Trans.*, 2003, 1083–1093.
63 Z. Sakhaei, S. Kundu, J. M. Donnelly, J. A. Bertke, W. Y. Kim and T. H. Warren, *Chem. Commun.*, Nitric Oxide Release via Oxygen Atom Transfer from Nitrite at Copper (II), 2017, **53**, 549–552.

64 L. M. R. Hill, B. F. Gherman, N. W. Aboelella, C. J. Cramer and W. B. Tolman, Electronic Tuning of *β*-Diketiminate Ligands with Fluorinated Substituents: Effects on the O_2-Reactivity of Mononuclear Cu(I) Complexes, *Dalton Trans.*, 2006, 4944–4953.
65 K. Huse, H. Weinert, C. Wölper and S. Schulz, Electronic Effect of a Perfluorinated *β*-Diketiminate Ligand on the Bonding Nature of Copper Carbonyl Complexes, *Dalton Trans.*, 2020, **49**, 9773–9780.
66 A. Kronast, M. Reiter, P. T. Altenbuchner, C. Jandl, A. Pöthig and B. Rieger, Electron-Deficient *β*-Diiminato-Zinc-Ethyl Complexes: Synthesis, Structure, and Reactivity in Ring-Opening Polymerization of Lactones, *Organometallics*, 2016, **35**, 681–685.
67 K. Huse, C. Wölper and S. Schulz, Main-Group-Metal and Transition-Metal Complexes Containing Fluorinated *β*-Diketiminate Ligands, *Eur. J. Inorg. Chem.*, 2018, **2018**, 3472–3480.
68 C. H. Zambrano, R. D. Profilet, J. E. Hill, P. E. Fanwick and I. P. Rothwell, Aryl Imido Complexes of the Group 4 Metals: Structural Aspects and Mechanistic Study of Formation, *Polyhedron*, 1993, **12**, 689–708.
69 C. Shimokawa, J. Teraoka, Y. Tachi and S. Itoh, A Functional Model for pMMO (Particulate Methane Monooxygenase): Hydroxylation of Alkanes with H_2O_2 Catalyzed by *β*-Diketiminatocopper(II) Complexes, *J. Inorg. Biochem.*, 2006, **100**, 1118–1127.
70 C. Shimokawa, Y. Tachi, N. Nishiwaki, M. Ariga and S. Itoh, Structural Characterization of Copper(I) Complexes Supported by *β*-Diketiminate Ligands with Different Substitution Patterns, *BCSJ*, 2006, **79**, 118–125.
71 C. Yang, L. Zhang, H. Li, Y. Guo, C. Jia, W. Zhu, F. Mo and X. Guo, Single-Molecule Electrical Spectroscopy of Organocatalysis, *Matter*, 2021, **4**, 2874–2885.
72 R. J. Lewis, M. Koy, M. Macino, M. Das, J. H. Carter, D. J. Morgan, T. E. Davies, J. B. Ernst, S. J. Freakley, F. Glorius and G. J. Hutchings, N-Heterocyclic Carbene Modified Palladium Catalysts for the Direct Synthesis of Hydrogen Peroxide, *J. Am. Chem. Soc.*, 2022, **144**, 15431–15436.
73 F. Wang, R. Tanaka, Z. Cai, Y. Nakayama and T. Shiono, Room-Temperature Suzuki–Miyaura Cross-Coupling Reaction with α-Diimine Pd(II) Catalysts, *Appl. Organomet. Chem.*, 2015, **29**, 771–776.
74 D. J. E. Spencer, N. W. Aboelella, A. M. Reynolds, P. L. Holland and W. B. Tolman, *β*-Diketiminate Ligand Backbone Structural Effects on Cu(I)/O_2 Reactivity: Unique Copper−Superoxo and Bis(μ-Oxo) Complexes, *J. Am. Chem. Soc.*, 2002, **124**, 2108–2109.
75 A. Bakhoda, O. E. Okoromoba, C. Greene, M. R. Boroujeni, J. A. Bertke and T. H. Warren, Three-Coordinate Copper(II) Alkynyl Complex in C–C Bond Formation: The Sesquicentennial of the Glaser Coupling, *J. Am. Chem. Soc.*, 2020, **142**, 18483–18490.